Title

Rietveld texture analysis from synchrotron diffraction images. II. Complex multiphase materials and diamond anvil cell experiments

Journal

Powder Diffraction, 29(3)

ISSN

0885-7156

Authors

Wenk, Hans-Rudolf
Lutterotti, Luca
Kaercher, Pamela
et al.

Publication Date

2014-09-01

DOI

10.1017/s0885715614000360

Peer reviewed

Rietveld texture analysis from synchrotron diffraction images. II. Complex multiphase materials and diamond anvil cell experiments

Hans-Rudolf Wenk,[1,a)] Luca Lutterotti,[2] Pamela Kaercher,[1] Waruntorn Kanitpanyacharoen,[1] Lowell Miyagi,[3] and Roman Vasin[1,4]
[1]*Department of Earth and Planetary Science, University of California, Berkeley, California*
[2]*Department of Industrial Engineering, University of Trento, Trento, Italy*
[3]*Department of Geology and Geophysics, University of Utah, Salt Lake City, Utah*
[4]*Frank Laboratory of Neutron Physics, Joint Institute for Nuclear Research, Dubna, Russia*

(Received 1 March 2013; accepted 7 March 2014)

Synchrotron X-ray diffraction images are increasingly used to characterize crystallographic preferred orientation distributions (texture) of fine-grained polyphase materials. Diffraction images can be analyzed quantitatively with the Rietveld method as implemented in the software package Materials Analysis Using Diffraction. Here we describe the analysis procedure for diffraction images collected with high energy X-rays for a complex, multiphase shale, and for those collected *in situ* in diamond anvil cells at high pressure and anisotropic stress. © *2014 International Centre for Diffraction Data.*
[doi:10.1017/S0885715614000360]

Key words: texture analysis, synchrotron diffraction, Rietveld method, shale, diamond anvil cell, ferropericlase

I. INTRODUCTION

In a companion paper (Lutterotti *et al.*, 2014), we have described the basic steps for texture analysis from synchrotron diffraction images with the Rietveld method, using the software Materials Analysis Using Diffraction (MAUD) (Lutterotti *et al.*, 1997). We assume that the reader is familiar with this introductory paper. In subsequent discussions, we will refer directly to sections in Lutterotti *et al.* (2014), e.g. as "Part I.IV". In this paper, we will discuss complexities that arise for samples with many phases and samples with a strong texture.

The first example here is sedimentary shale composed of multiple types of minerals, with different volume fractions, microstructures, and orientation distributions (ODs). The second complex sample is ferropericlase (Mg,Fe)O, measured *in situ* at ultrahigh pressure and anisotropic stress conditions in a diamond anvil cell (DAC). We can provide only an outline of analysis procedures, but the reader should keep in mind that the Rietveld method and its implementation in MAUD is very general and lends itself to many applications, each of which requires slightly different approaches, modifications, and application of specific models. With the two examples we try to introduce several of the capabilities of MAUD that a user may consider for a particular sample, including sample rotations, background models and symmetry transformations. Step-by-step guides are provided as two appendices, which can be freely downloaded along with the corresponding data files from the internet (http://PD-journal.htm).

[a)]Author to whom correspondence should be addressed. Electronic mail: wenk@berkeley.edu

II. SHALE AS AN EXAMPLE OF A COMPLEX POLYPHASE MATERIAL

A. Diffraction experiment

Shale is a sedimentary rock and composed of a wide variety of minerals. Sheet silicates comprise a large volume fraction of shales and align preferentially parallel to the bedding plane during sedimentation and compaction. Crystallographic preferred orientation (CPO) of phyllosilicates is of great interest, because it is the primary cause of elastic anisotropy observed during seismic prospecting of oil and gas deposits. Thus several studies have focused on improving synchrotron X-ray techniques to quantify textures and microstructures of shales (e.g., Wenk *et al.*, 2008; Lutterotti *et al.*, 2010; Kanitpanyacharoen *et al.*, 2011, 2012a; Vasin *et al.*, 2013).

For this tutorial we use a sample of Kimmeridge shale from the North Sea, UK (Hornby, 1998; Vasin *et al.*, 2013). The sample is a slab, 2 mm thick [Figure 1(a)]. It was measured at the APS high-energy beamline ID-11-C during the same session as the nickel coin discussed in the companion paper (Lutterotti *et al.*, 2014). The wavelength was 0.107 98 Å, and the beam size 0.5 × 0.5 mm. Therefore, the same instrument parameters could be applied which were obtained by refining the CeO_2 standard (see Part I.III). However, samples can shift, so here we will use a slightly different approach as described in detail in Appendix I. This will illustrate the flexibility of MAUD in assigning sample and image orientations relative to the MAUD coordinate system [Figure 1(b)]. During X-ray exposure the sample was translated along the horizontal axis from −2.5 to +2.5 mm to increase the probed volume, and rotated around the horizontal axis (Figure 1 in Lutterotti *et al.*, 2014), from −45° to +45° in 15° increments (i.e., there are seven diffraction images) to obtain adequate pole figure coverage. For the coin we used Y_M as the rotation axis, here we will use Z_M [Figure 1(b)].

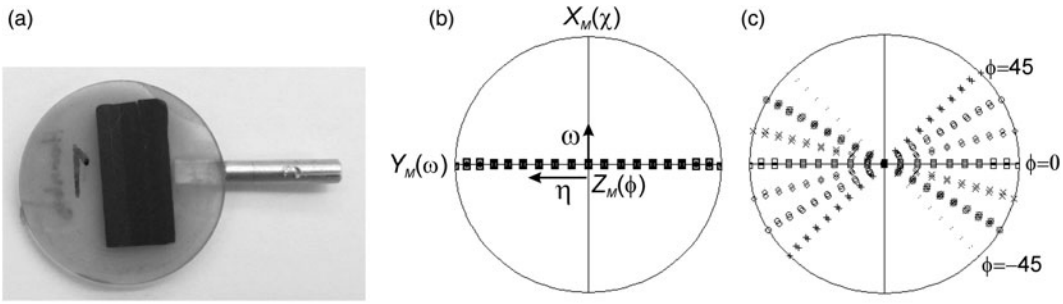

Figure 1. (a) Slab of shale embedded in epoxy and mounted on a pin. (b) Pole figure coverage with a single image, bedding plane normal is in the center of the pole figure. When fiber symmetry is imposed, each point covers a circle. (c) Coverage with seven images recorded at different sample rotations φ around the Z_M axis.

The reason for the change in coordinate systems is that this way the pole to the bedding plane of the shale is located in the center of the pole figure and axial symmetry can be imposed. Since the texture describes the preferred orientation of crystals relative to sample coordinates, care must be taken that this relationship is not lost during rotations.

Images were collected with a Perkin Elmer amorphous silicon detector with dimensions of 2048 × 2048 pixels and a pixel size of 200 × 200 μm. The detector was approximately 1850 mm from the sample. Figure 2(a) shows a diffraction image with many Debye-rings from at least six major phases at different 2θ angles. Several rings display strong intensity variations due to preferred orientation.

B. Preliminary analysis for axial symmetry using one image

Refining seven images simultaneously with a number of low-symmetry phases is time-consuming [two-dimensional (2D) diffraction images are integrated in angular azimuthal increments, resulting in a total of several hundred patterns]. Thus it is more efficient to start with only one image measured at $\varphi = 0°$ [coverage in Figure 1(b)]. Later, we will add the other images in different datasets to complete the analysis [coverage in Figure 1(c)]. The procedure with a single image is justified, because shale textures have approximately axial (fiber) symmetry about the bedding plane normal (transverse isotropy). By imposing this sample symmetry, complete pole figure coverage is obtained with only one dataset. If the texture is not too strong, one can initially assume a random orientation to simplify the first refinement steps and introduce the texture later with the additional images. In case of a very strong texture, we have to work from the start with all images and a complete texture model, but this is not the case for the shale example.

We start from an instrument calibrated with the CeO_2 standard and use the same procedure as for the coin analysis (Part I.IV) to load and integrate the first image. Compared to the coin, we do not rotate the image 90° counterclockwise in ImageJ before processing, so that the horizontal axis is in the center (Z_M) for the shale sample; in this way the bedding plane normal is in the center of the pole figure [see Figures 1(b) and 1(c)]. Since the texture of shale is smoother than the coin [see Figure 2(a)] we can employ a larger integration step of 10°; this reduces the total amount of data to analyze without loss of information and with an increase in speed of the computation. Initially we restrict the refinement range to $2\theta = 0.3$–$3.0°$ since shale contains several low-symmetry phases with many diffraction peaks that overlap at higher 2θ. Those peaks do not provide much information for texture analysis. Restricting the range greatly speeds up the computation. If necessary, the range can be enlarged at the end of the refinement.

Figure 3 (bottom) displays the stack of experimental diffraction patterns taken at each 10° increment in eta (η). The pole figure coverage is shown in Figure 1(b) with the pole to the bedding plane at Z_M (φ rotation axis).

We use a fourth-order polynomial background common to all patterns (5 coefficients). However, we must also correct

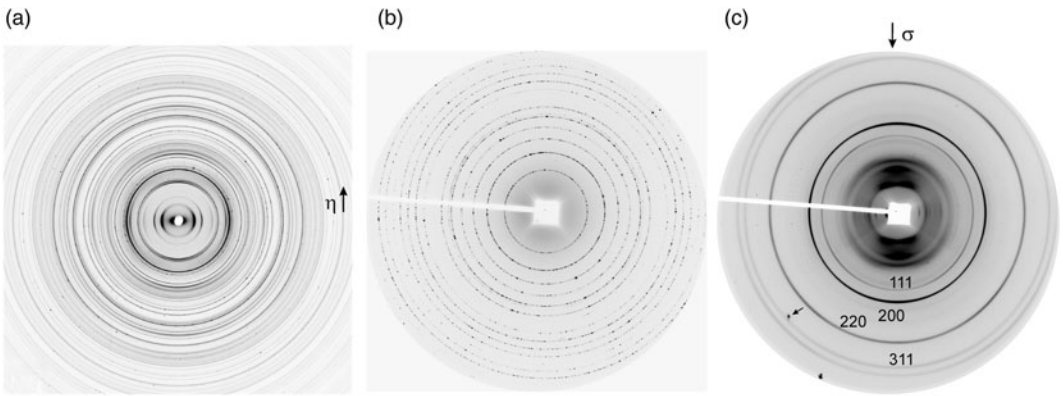

Figure 2. 2D synchrotron diffraction images. (a) Kimmeridge shale with many phases, some with strong preferred orientation. (b) LaB_6 standard used for the DAC experiment, rather coarse-grained and with some impurities. (c) Radial diffraction DAC experiment on ferropericlase. Arrow points to a diffraction spot from diamond. The compression direction is vertical.

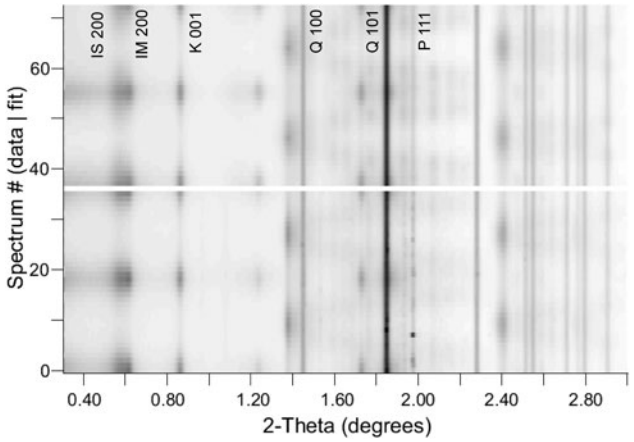

Figure 3. Stack of diffraction patterns for Kimmeridge shale, $\varphi = 0°$ tilt image. Experimental data at bottom and Rietveld fit on top. Some diffraction for lines for illite-smectite (IS), illite-mica (IM), kaolinite (K), quartz (Q) and pyrite (P) are labeled.

for small angle scattering from platelet-shaped phyllosilicate nanoparticles, which is most visible in the diffraction image at very low angles ($2\theta \approx 0.1$–$0.2°$), near the beamstop [Figure 2(a)]. Since these platelets are oriented, small angle scattering displays azimuthal intensity variations. The broad low-angle peak extends as elevated background to the first diffraction peaks of phyllosilicates ($2\theta \approx 0.3$–$0.6°$) (Figure 3). To fit this peak, we use two symmetrical background peaks, which are pseudo-Voigt functions that can be positioned arbitrarily in a dataset at any coordinates. The principal one is 2θ [parameters are intensity, 2θ position, half-width at half-maximum (HWHM) in 2θ, and the Gaussian content], but it may span over η (adding a position, HWHM and Gaussian content in η) as well as position angles (χ, φ). Background peaks are useful to model some well-defined bumps occurring in images that do not belong to diffraction from a phase. For details, see the tutorial in Appendix 1.

We limit the refinement to the five major phases: quartz, pyrite, kaolinite, illite-mica, and illite-smectite. There are minor phases such as feldspars with <5% volume and no significant texture. Quartz and pyrite structures can be found in the Crystallography Open Database (Gražulis *et al.*, 2009) or in the small database included with MAUD (structures.mdb). We added the following structures to this tutorial: triclinic kaolinite (Bish and Von Dreele, 1989), monoclinic illite-mica (Gualtieri, 2000), and monoclinic illite-smectite (Plançon *et al.*, 1985). The corresponding Crystallographic Information Files (.cif) are available in the on-line material supplied with the tutorial. For monoclinic phases, the first monoclinic setting has to be used to work with texture (Matthies and Wenk, 2009). All texture models implemented in MAUD have been written for the monoclinic "*c-unique*" setting (i.e., $\alpha = \beta = 90°$ and $\gamma \neq 90°$); otherwise crystal symmetries are not imposed correctly in orientation space. In MAUD one can change from one setting to another simply by editing the phase and under the "General" tab, selecting the desired setting in the "Space Group" drop-down list. Lattice parameters and atomic positions are adjusted automatically, for example, for the illite-mica phase changing from MAUD settings of *C*2/*c*:*b*1 to *C*2/*c*:*c*1, which selects *c* for the unique (twofold) axis. Note that the "1" at the end of the space group symbol stands for the first origin and the setting letter is after the colon. The provided .cif file for illite-smectite is already in the first (*c*-unique) setting.

When multiple phases are entered, MAUD automatically assigns to each added new phase the volume fraction equal to 1/(the total number of phases in the sample). In Rietveld programs, each phase has an assigned scale factor, and each scale factor is optimized during the refinement. Then, from the refined scale factors, the volume and weight fractions of the phases are computed. In addition to volume fraction, the scale factor contains information about the beam intensity and other factors such as absorption, yet it is treated as a unique parameter. If the phases are textured we need an approach that models the sample correctly and uses phase fractions, beam intensities, and absorption corrections (Lutterotti *et al.*, 2010), which all contribute to peak intensities and thus may complicate intensity. In our final model, fitting to data from all seven images, we will have a beam intensity parameter for each image, but all patterns in each image have the same beam intensity. Furthermore, we refine the phase fractions for all phases minus one. MAUD imposes that the sum of all phase fractions should be equal to 1 and enforces the volume fraction of the unrefined phase to be the complement to 1.

With a complex sample such as this shale, it is important to provide reasonable initial estimates of phase volume fractions. This avoids divergence of the solution in the initial steps of the least-squares algorithm. Weight fractions are calculated automatically by MAUD, using the provided atomic structure and unit-cell parameters.

For texture, with the initial simplified model using only one image, we need to impose the axial symmetry that MAUD always imposes around the center of the pole figure [Figures 1(b) and 1(c); for the MAUD angle convention and transformations, see also Grässlin *et al.*, 2013 and Figure 4(a) in Part I].

After manually adjusting some parameters, such as unit-cell parameters, beam intensity, and background to better fit the experimental patterns (in the parameter list in the MAUD main window, adjust numbers in column "Value"), we start by refining some basic parameters. In the Rietveld refinement procedure, it is always better to avoid refining too many parameters at the beginning and to "guide" the program to the solution. There are normally three major steps to follow: (1) refine background parameters and intensities (scale factors or in MAUD beam intensities and phase fractions); (2) refinement of parameters connected to the peak positions (unit-cell parameters and 2θ errors); and (3) refine microstructural parameters such as crystallite sizes and microstrain. While doing subsequent refinements, one should not change the setting for the refinement of previously refined parameters; the goal is to slowly add additional parameters to the fit. When do we refine texture-related parameters? If the texture is smooth, or weak, it is done at the end (a fourth step), to avoid refining texture instead of some other parameter that could impose intensity variations (e.g., absorption). However, if the texture is sufficiently strong we introduce the texture refinement along with the refinement of intensities in the first step, as long as diffraction peak positions are well constrained. The crystal structure details (e.g., atomic positions and even lattice parameters) should be refined only if necessary and only for phases with sufficient volume fractions and visible peaks. Also, one should use only a single overall

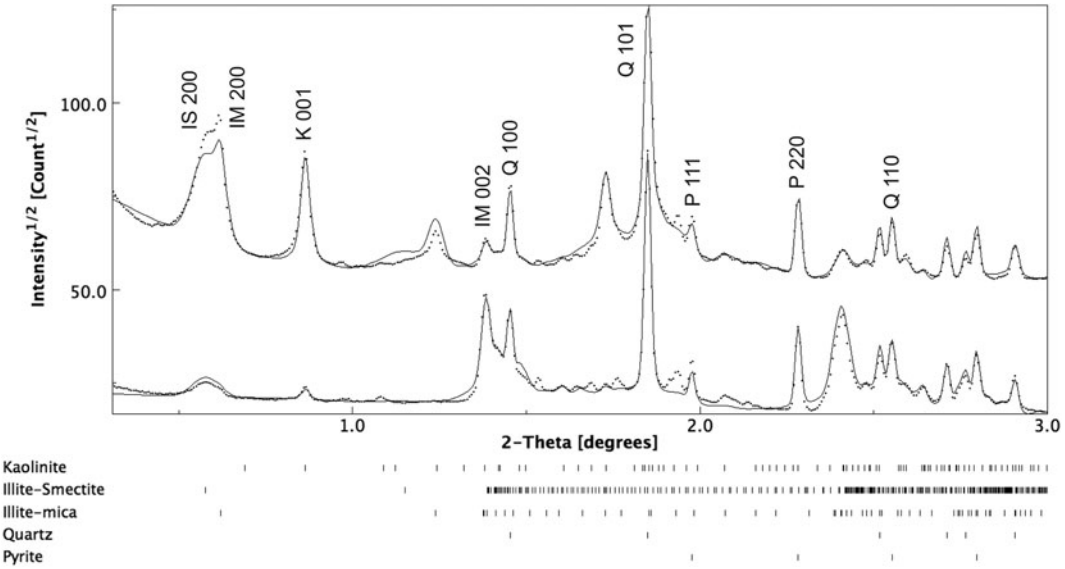

Figure 4. Two diffraction patterns of Kimmeridge shale with scattering lattice planes parallel to bedding plane on top and perpendicular to it at bottom. Crosses are measured data and line is Rietveld fit. Below the patterns is a list of contributing phases and their corresponding diffraction peak positions are marked with ticks. Some diffraction peaks are labeled (IS, illite/smectite; IM, illite/muscovite; Q, quartz; P, pyrite).

atomic displacement parameter (B factor, which is sometimes called temperature factor) by clicking on "Bound B factor" button in the parameter list. When working at high-energy X-rays and very low 2θ angles (available 2θ range is restricted) the data are practically insensitive to B factors. As in the case of the coin in Part I, we should refine the x and y image centering errors as we cannot assure that the CeO_2 calibrant was in the center of the beam, whereas for the shale the beam is inside the sample.

Looking at Figure 3, diffraction peaks of kaolinite (K), illite-mica (IM), and illite-smectite (IS) show strong η-dependent intensity variations indicative of texture. The intensities of the quartz (Q) and pyrite (P) diffraction peaks are almost constant, except for several increased intensity spots because of scattering from larger grains (e.g., P 111 peak). Thus, we only refined preferred orientations of the three phyllosilicates but not of quartz and pyrite. We used the E-WIMV model (Part I.IV) for the kaolinite and the illite-mica with a rather large cell size of 10° in orientation, space given the smooth character of the texture. In general, one should not select a smaller cell size than the measured grid in patterns (in this case it is defined mostly by 10° integration sectors).

For illite-smectite with a well-defined orientation, we use the so-called standard functions method to introduce this capability (Matthies *et al.*, 1987 and implemented in MAUD by Lutterotti *et al.*, 2007). The advantage of this approach is that we can describe preferred orientation with some well-defined functions with only few parameters. MAUD implements Gaussian or Lorentzian fiber components (having a fiber symmetry character) and spherical components (also Gaussian, Lorentzian, or mixed). For both types of components, we refine their position in the orientation space, width (in degrees), and Gaussian or Lorentzian character (a single mixing parameter). For the position, the fiber component is defined by the fiber axis orientation with respect to the sample normal (azimuthal PhiY and polar angle ThetaY) and the orientation axis in the unit cell (also two angles: the azimuthal angle around the c-axis PhiH and the polar angle starting from the c-axis ThetaH; see for analogy the angles Φ and β in the appendix of Popa, 1992). Standard function texture corrections are very quick to compute and converge rapidly. Another advantage of the standard functions is that they can model very smooth or very strong textures up to epitaxial films, or even single-crystal-like patterns, depending on the width of the component. We defined the fiber axis here parallel to the bedding plane normal [corresponding azimuthal and polar angles are equal to zero, Figure 1(c)]. For the crystallographic texture orientation, we know that the $h00$ maximum is in the center of the pole figure (monoclinic first setting) and we set the azimuth PhiH to 90° and the polar angle ThetaH to 0°. In this case, we do not refine the orientation angles, as they do not deviate from the imposed starting values, and only the width and Gaussian/Lorentzian mixing parameter of the fiber component will be refined.

The illite-smectite peaks are unusually broad and asymmetric (Figure 4) because of turbostratic disorder, which is typical of clay minerals. This kind of disorder can be described with the Ufer single-layer model (Ufer *et al.*, 2004). The model is very effective in reproducing the asymmetric broadening caused by the turbostratic disorder and can be coupled with the texture analysis (Lutterotti *et al.*, 2010). We only need to define the faulting direction ($h00$) for the smectite and the supercell dimension to approximate the disordered structure. We choose ten times the a-axis (first monoclinic setting) as a sufficient value to model the disorder.

In Figure 3 (top), we can see the resulting 2D plot after the initial refinement with one image and the agreement with the experiment is very good (Figure 3, bottom). Figure 4 shows two individual patterns, one with scattering vectors parallel to, and the other perpendicular to the bedding plane normal and also good agreement for both is observed here. The tick-marks at the bottom denote peaks belonging to each phase. This is the quality that fit users should aim for. Table I lists refined volume and weight fractions for the phases and Table II gives information about the texture. Corresponding

TABLE I. Phase volume and weight fractions of minerals in shale (in %), with and without imposed axial symmetry of texture, and also using full 2θ range.

	Vol. axial	Wt. axial	Vol. no symm	Wt. no symm	Vol. full range	Wt. full range
Kaolinite	9.9(2)	9.1(2)	8.7(1)	8.1(1)	11.8(1)	10.8(1)
Illite-mica	29.8(5)	29.7(5)	32.5(2)	32.9(2)	27.0(1)	27.0(1)
Illite-smectite	24.5(7)	22.8(6)	31.8(2)	29.7(2)	32.6(2)	31.7(2)
Quartz	30.6(5)	29.1(5)	22.9(1)	21.9(1)	24.7(1)	23.5(1)
Pyrite	5.2(5)	9.3(8)	4.1(1)	7.4(1)	3.9(1)	7.0(1)

TABLE II. Texture information for phyllosilicates in shale after processing in BEARTEX, pole densities in m.r.d., with and without imposed axial symmetry of texture, and also using full 2θ range.

	Max axial	Min axial	Max no symm	Min no symm	Max full range	Min full range
Kaolinite 001	6.84	0.22	5.14	0.31	4.44	0.15
Illite-mica 100	8.50	0.12	7.78	0.25	9.73	0.21
Illite-smectite 100	3.83	0.39	3.70	0.30	3.22	0.32

TABLE III. Texture information for ferropericlase at 39.6 GPa; pole densities of different pole figures and inverse pole figure (IPF) in m.r.d. Numbers in parentheses are after exporting the ODF to BEARTEX.

	Max	Min	Max no symm	Min no symm
100	2.64 (2.74)	0.67 (0.73)	2.57	0.55
110	1.12 (1.26)	0.75 (0.86)	1.47	0.59
111	1.12 (1.26)	0.51 (0.53)	1.55	0.44
IPF	3.19 (2.74)	0.51 (0.53)		

pole figures are shown in Figure 5(a) in equal-area projection. Note that illite-mica has the strongest texture and illite-smectite shows the broadest OD. The *R*-factors, which measure the overall goodness of fit between the model and experimental data, were: $R_w = 12.5\%$ and $R_b = 8.9\%$ for the single image refinement. In general, *R*-factors smaller than 15% typically demonstrate a very good refinement.

C. Analysis without imposing texture symmetry

With this preliminary refinement, we can add the other six diffraction images and proceed with the full analysis. In the end we can also enlarge the refinement range.

With all the seven images rotated in 15° φ increments around Z_M and integrated in 10° sectors around η, the pole figure coverage is now as shown in Figure 1(c). With the larger OD coverage we can analyze the full texture without imposing sample symmetry and use E-WIMV, also for the illite-smectite. In E-WIMV, the default in MAUD is to use all the reflections in the computing range. Contrary to the classical WIMV and pole figure texture analysis, in Rietveld/E-WIMV the pole figure value is weighted using the square root of the theoretical integral intensity of the reflection [Eq. (2) in Lutterotti *et al.*, 2004]. In this case, if we use the full range, the three textured phases have many overlapped and very weak reflections, even up to 3° in 2θ. Weak overlapped reflections do not contribute significantly to the OD and introduce noise. The texture analysis improves if such reflections are not used, as long as there is no problem with coverage. E-WIMV and WIMV have an option to reject reflections with either small intensities relative to the strongest

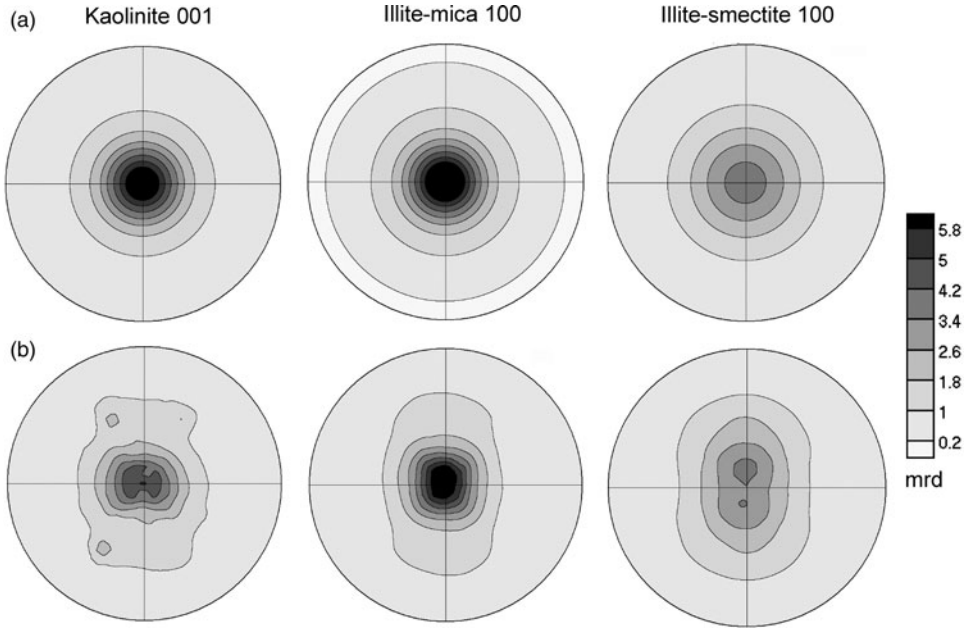

Figure 5. Pole figures of basal planes of kaolinite, illite-mica and illite-smectite for Kimmeridge shale after exporting the ODs from MAUD and processing them with BEARTEX. (a) Derived from a single image, imposing fiber symmetry. (b) Result for seven images without imposing symmetry. The corresponding pole figure coverage is shown in Figure 1(c). Equal area projection on the bedding plane, contours in multiples of a random distribution.

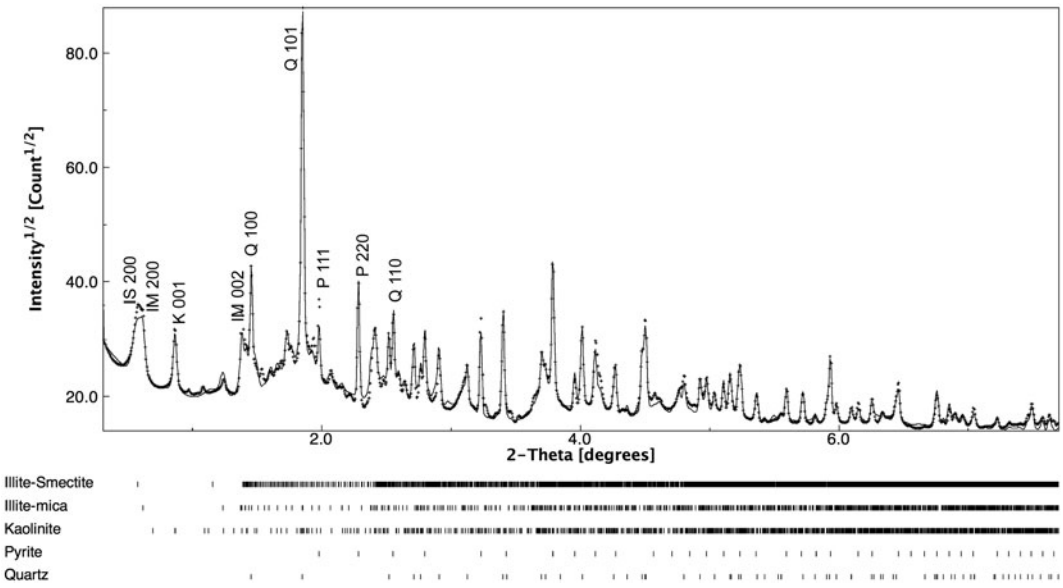

Figure 6. Cumulative plot for all patterns of the $\varphi = 0$ image at the end of refinement cycles with seven images, full 2θ range. Dots are experimental data and line is Rietveld fit. Some diffraction peaks are labeled (IS, illite/smectite; IM, illite/muscovite; Q, quartz; P, pyrite).

reflection or *d*-spacings lower than a threshold value. In the present analysis, we use these options and avoid reflections with intensity <2% of the strongest reflection and with *d*-spacings smaller than 1.5 Å.

Figure 6 shows the final fit to all seven diffraction images with a cumulative plot of all patterns for the dataset $\varphi = 0°$ and a 2θ range 0.4–7.8°. At low angles kaolinite, illite-mica and illite-smectite peaks dominate the pattern, whereas at high angles quartz and pyrite dominate. In a case like this, it is important to check the B factors. Wrong B factors for the pyrite/quartz and the other low angle phases may lead to angular-dependent errors that will greatly affect the phase fractions between the "low angle" and "high angle" phases.

Pole figures of phyllosilicates, corresponding to those in Figure 5(a), but without imposing symmetry, are shown in Figure 5(b). Note that these pole figures look slightly different from what the reader might see in MAUD. This is because the OD data have been exported from MAUD and were replotted in the software BEARTEX (Wenk *et al.*, 1998), in order to alleviate artifacts from the cell structure by smoothing and plotting all pole figures on the same scale. In Figure 7, we also show pole figures (100) of kaolinite and (010) of illite-mica and illite-smectite that display a peripheral circle.

In this tutorial presentation, we have started with a single image and imposed axial symmetry, then progressed to many images with no symmetry. This was done to progress from a simple to a more complex analysis. In reality one may want to progress the opposite way: first, with many images, verifying sample symmetry; second, performing necessary sample rotations to bring sample symmetry axes to coincidence with MAUD coordinates, and finally imposing symmetry with one image (for axial symmetry) or several images for more complex sample symmetries.

Pole figure coverage is an important issue, particularly for phases with low crystal symmetry. Shales have very special textures with a maximum pole density corresponding to sheet silicate platelets lying in the bedding plane (Figure 5). This maximum has been well sampled with the present coverage [Figure 1(c)]. However, directions in the bedding plane and particularly in the X_M direction have minimal coverage (Figure 7). The pole figures in Figure 5(b) show minor deviations from axial symmetry, particularly an elongation of the pole figure maxima in the vertical direction for (001) in kaolinite and (100) in illite-mica and illite-smectite. This distortion extends into the blind region of coverage [Figure 1(c)] and may be an artifact. This is further supported by the fact that the maximum pole densities are higher if the axial

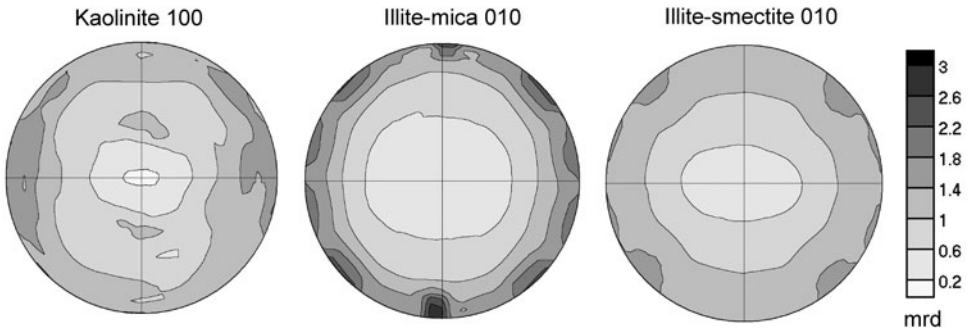

Figure 7. Pole figures 100 of kaolinite and 010 of illite-mica and illite-smectite for Kimmeridge shale without imposing sample symmetry. The corresponding pole figure coverage is shown in Figure 1(c). Equal area projection on the bedding plane, contours in multiples of a random distribution.

symmetry is imposed (Table II). Only additional measurements with rotations around other sample axes and combining the data could refine the preferred orientation pattern, but this goes beyond the purpose of this tutorial. One may also want to use a different sample geometry, such as a cylinder instead of a slab, and rotate it from $\varphi = -90°$ to $\varphi = +90°$, collecting 13 images.

Phase volume fractions for Kimmeridge shale without imposing sample symmetry are compared in Table I with results for axial symmetry. They are very similar. For the Kimmeridge shale, the final Rietveld R_w factor is 10.9% (R_b = 8.2%) for the refinement in the 2θ range up to 3°. A few peaks are missing from the calculated diffraction pattern, some are too intense, and some have wrong shapes (e.g., Figures 3 and 4). The missing peaks are mostly because of a feldspar phase that could be entered into the refinement, but we opt to not do so. Anisotropic crystallite shapes and microstrains could also be imposed for phyllosilicates. We have used a CeO_2 powder to refine instrumental parameters (Part I), but CeO_2 has no diffraction peaks at $2\theta < 2°$. Thus the function describing the instrumental part of diffraction peak broadening (especially the asymmetry) is poorly constrained for this shale with diffraction peaks down to $2\theta \approx 0.5°$. Parts of the instrumental peak shape function (the asymmetry) can be refined, as has been done for the full range analysis (see Figure 6). The final R_w for the refinement of the full range and all seven images was reduced from the one image refinement to 10.3% (R_b = 7.4%), which is a very good value, given the number of patterns and complexity of the phases.

III. DAC IN RADIAL DIFFRACTION GEOMETRY

A. Experiment

Rietveld texture analysis of synchrotron diffraction images can be applied to study *in situ* deformation at high pressures with a DAC in radial diffraction geometry (rDAC) (e.g., Merkel *et al.*, 2002; Wenk *et al.*, 2006). This proves to be an important method to determine deformation mechanisms at ultrahigh pressures, as in the deep Earth (e.g., Miyagi *et al.*, 2010) to explain observed seismic anisotropy in the lower mantle and inner core, and to study crystal orientation changes during phase transformations (e.g., Miyagi *et al.*, 2008; Kaercher *et al.,* 2012; Kanitpanyacharoen *et al.*, 2012b). The method can also be applied to analyze data from multi-anvil experiments such as D-DIA (e.g., Wenk *et al.*, 2005, 2013).

The geometry of a typical rDAC deformation experiment is shown in Figures 8(a) and 8(b). Diamonds not only impose pressure, but also deviatoric stress that deforms crystals in the aggregate. The diamond cell is set up in radial rather than axial geometry, i.e. the X-ray beam passes through the sample perpendicular to the compression direction [Figure 8(b)] so that the diffraction image records reflections from lattice planes oriented from parallel to perpendicular to compression [Figure 2(c)]. Preferred orientation is expressed in the azimuthal intensity variations, similar to the images of the shale [Figure 2 (a)]. Many DAC experiments, not concerned with stress and texture, use axial geometry, where the X-ray passes through the diamonds and parallel to the compression direction.

rDAC experiments have been performed at room temperature to pressures as high as 200 GPa on iron (Wenk *et al.*, 2000) and 185 GPa on $MgSiO_3$ post-perovskite (Miyagi *et al.*, 2010). More recently texture measurements have been made in the rDAC on ferropericlase (Mg,Fe)O at 2273 K and ≈ 65 GPa, using a combination of resistive and laser heating (Miyagi *et al.*, 2013).

Contrary to the coin and shale experiments, we must take into account changes with pressure, and particularly the macroscopic stress field, which imposes anisotropic elastic distortions of the lattice. As an example we use ferropericlase (magnesiowuestite), which has been previously investigated with rDAC experiments (e.g., Merkel *et al.*, 2002; Kunz *et al.*, 2007; Lin *et al.*, 2009; Kaercher *et al.*, 2012). This particular sample $(Mg_{0.75}Fe_{0.25})O$ has been described by Kunz *et al.* (2007).

The rDAC experiment was performed at the high-pressure beamline 12.2.2. of the Advanced Light Source at Lawrence Berkeley National Laboratory. Ferropericlase powder was loaded into a boron-kapton gasket. The initial sample diameter was 80 μm with a starting thickness of 50 μm. The sample was compressed in an rDAC, using diamond anvils with 300 μm diameter culets [Figure 8(c)]. Diffraction images were recorded with a Mar345 image plate detector, with dimensions of 3450 × 3450 and a pixel size of 100 × 100 μm, positioned approximately 285 mm from the sample with an X-ray wavelength of 0.495 94 Å.

There are two immediate complications. First, the beam passes not just through the sample, but also through a gasket, which is needed to maintain pressure. Thus there are additional diffraction lines from the gasket material, especially at low angles [Figure 2(c)]. Gaskets for radial DAC experiments must be made of materials that scatter as little as possible. At lower pressures, amorphous boron (<100 GPa) has been used, while at higher pressure, cubic boron nitride or beryllium have been used. For beryllium, which scatters more, it is advantageous to tilt the cell to have minimum beam interference. If the cell is tilted significantly, the tilt needs to be accounted for by entering the appropriate sample rotation angles in MAUD. Bright diffraction spots from the diamond may also appear in the diffraction pattern. In fact, the large spot on the left side of Figure 2(c) (arrow) is because of diamond. This effect can be minimized by slightly rotating or tilting the DAC. Intense spots can also be masked in image processing.

A second complication is imposed anisotropic elastic strain. Lattice plane spacings are smaller in the compression direction and larger perpendicular to the compression axis. Thus, the Debye rings appear not as circles but as ellipses. The resulting sinusoidal variations of the diffraction peak positions with azimuthal angle are best seen with remapped coordinates, as unrolled images [Figure 9(a), bottom].

Ideally the rDAC data analysis should be performed immediately during the DAC experiment, at least through the basic steps. This is necessary, for example to refine lattice parameters and be able to estimate pressure from the equation of state. Thus parameter files with general information should be set up in advance.

B. Initial setup

1. Instrument calibration

Before analyzing the ferropericlase diffraction pattern, instrument parameters have to be refined with a reference sample. In this case LaB_6 was used, adopting the NIST-certified unit-cell parameter a = 4.156 89 Å [Figure 2(b)]. As

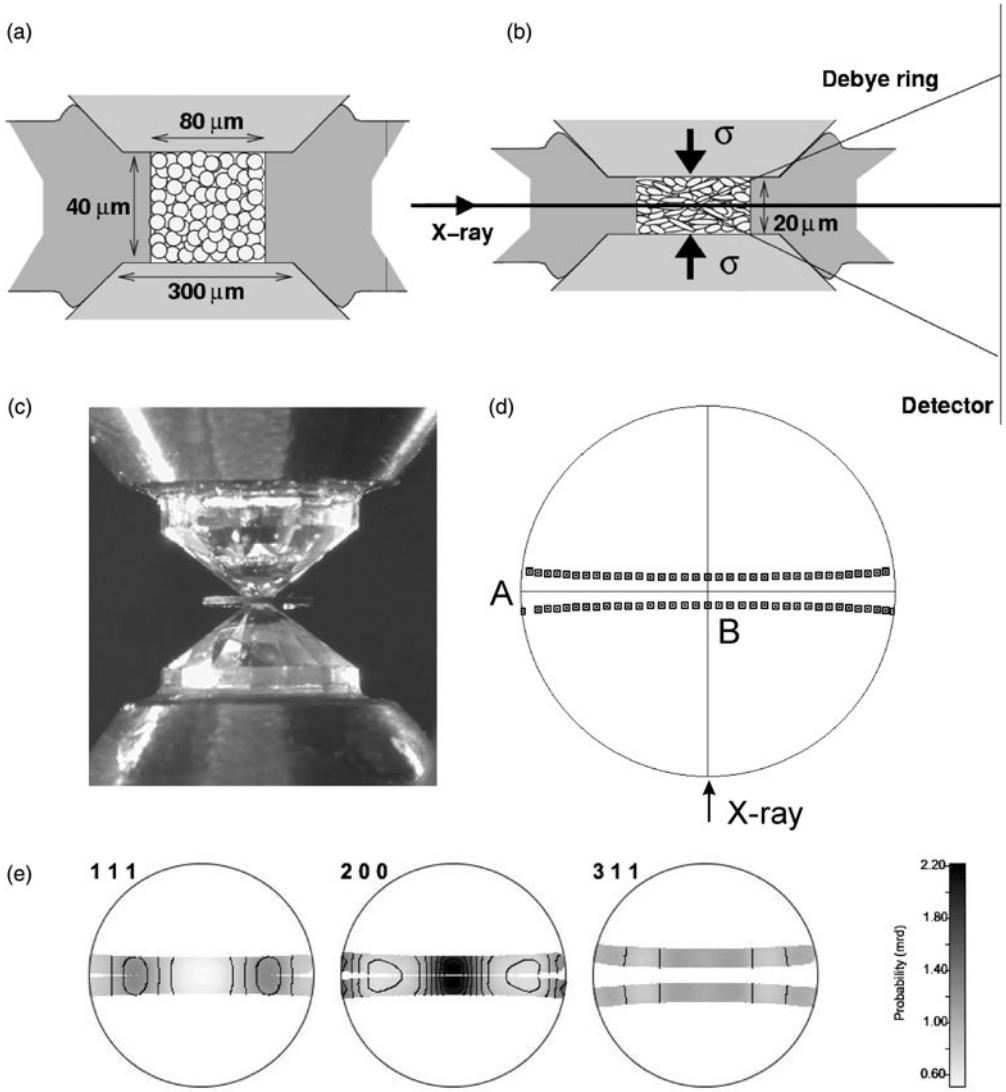

Figure 8. (a, b) Schematic sketch illustrating the geometry of deformation experiments in a DAC in radial diffraction geometry. (c) Actual diamond culets compressing a sample contained by a gasket. (d) Pole figure coverage for the ferropericlase DAC experiment (equal area projection, upper hemisphere). A gap is visible where one pattern is disabled because of the beam stop blocking diffracted X-rays. Direction of incident X-ray beam is shown by arrow. (e) Experimental pole figure data for three reflections.

with CeO_2, the unit-cell parameter and the wavelength are kept fixed, while detector centering, tilts and distance from the sample are refined. See Appendix 2 for a step-by-step guide for calibrating instrument parameters in MAUD. The MAUD procedure has been used for the detector calibration and subsequent analysis with the ferropericlase in order to separate the effects on the Debye rings because of detector misalignment from the applied stresses. For the refinement of instrument parameters, we did not use any asymmetry in the Caglioti parameters as the measured diffraction peaks are far from the image center and thus do not show any broadening asymmetry. Also, in this case there is no η-angle-dependent diffraction peak broadening.

During the refinement of the LaB_6 standard provided by ALS, we noted additional peaks due to sample contamination, of which some peaks are very small and can simply be neglected. One peak at $2\theta \approx 15.78°$ is significant and therefore, we excluded the region 2θ 15.5–16° from the analysis. An additional complication arises from the coarse nature of the standard with respect to the small beam size, causing some intense "spots" originating from diffraction from a few very large grains [Figure 2(b)]. In general, it would be advisable not to use such a coarse-grained impure standard or to be able to spin the sample to avoid graininess problems. We used a so-called Le Bail refinement (Le Bail *et al.*, 1988) but permitting different values of the intensities/structure factors for each pattern. In MAUD a Le Bail structure factor extraction is done with the restriction that different patterns (same instrument) share the same structure factors. Here we want to allow the variation of peak intensity with azimuthal angle. This is done in MAUD using the texture model "Arbitrary Texture", where intensity variations are neither bound to an OD, nor to a crystal structure.

Next we start processing the ferropericlase DAC image. Because of the anvil cell geometry, we cannot tilt the sample, and the number of Debye rings and their extension is limited. Since stresses are of interest and with the small angular range, it is important to have a very good detector calibration to correctly separate the effect of the detector misalignment from the anisotropic stress on the sample.

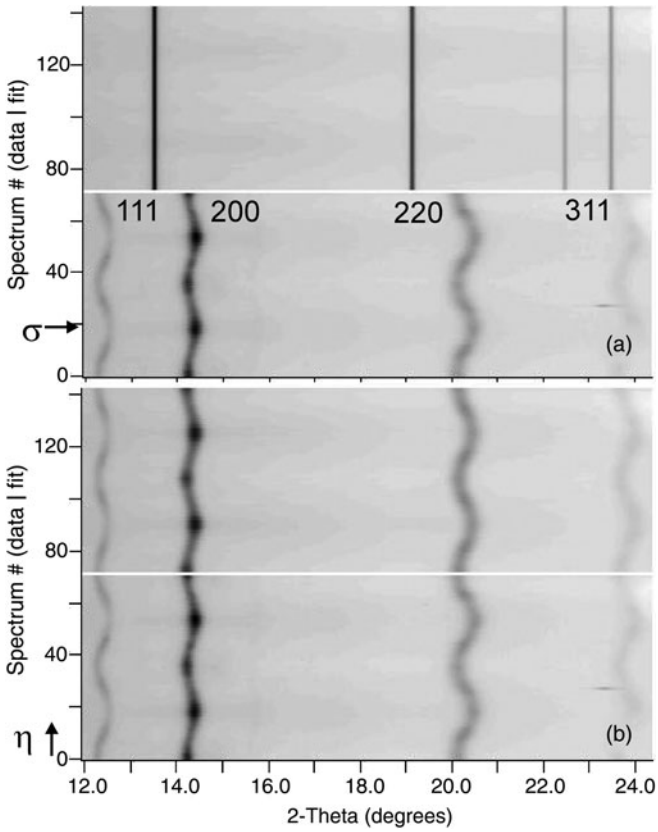

Figure 9. Measured (bottom) and calculated (top) diffraction patterns for ferropericlase; (a) at the beginning of the refinement. Lattice parameters are wrong and there is no texture or anisotropic stress in the model. Also note the black diffraction spot from diamond at $2\theta = 23.5°$. (b) At the end of the refinement there is an excellent match in position, width and intensity. The compression direction σ is indicated by the black arrow in (a) (larger 2θ angle corresponding to smaller d-spacing).

We use the instrument calibration values obtained by the LaB_6 refinement and process the DAC image as described in Part I. We integrated the image in 5° sectors to generate 72 patterns. This smaller integration step is essential in this case, because the texture is strong and significant peak shifts occur due to anisotropic stress. If the integration step is too large, the variations of diffraction peak positions and intensities can not be accounted for properly. We choose a computation range from 6° to 24° in 2θ in order to include the four prominent diffraction peaks (111), (200), (220), and (311) of ferropericlase (Figure 9) and to exclude diffractions from gasket material. In Figure 9(a) (bottom), there is a sharp spot at $2\theta \approx 23.8°$. This is a diffraction spot from the diamond anvil [Figure 2(b), arrow]. However, since it is not too intense, we do not need to exclude this from the diffraction pattern as it does not significantly affect the refinement. In other cases, if spots from the diamond anvils influence the results, then regions containing diffraction from the anvils should be disabled. A test, by running refinement both including and excluding the pattern with the single-crystal spot, can be done to check for its influence. Spots can also be eliminated from the diffraction images by image preprocessing (e.g., in ImageJ).

The waviness of the diffraction lines [Figure 9(a), bottom] is not due to a centering or tilting error of the detector, but to the deviatoric part of the applied stress, i.e. the difference between the compression along the main compression axis of the anvil cell (indicated by arrow: larger 2θ, smaller d) and the transverse direction. Fitting of this effect will be discussed below.

Setting up the background in rDAC experiments can be difficult, because of scattering and absorption from gaskets and DAC [Figure 2(c)]. In this case, it is best to use an interpolated background (independent for each pattern). A first positioning of interpolation points is done automatically using an algorithm described by Sonneveld and Visser (1975) and selecting only the starting interval between points and the number of iterations of the algorithm optimizing the background points' position. After the automatic positioning by the routine, the number and positions of the points can be adjusted manually, but in the case of many patterns this may be time consuming as it must be done for each pattern. The use of the algorithm and the presence of patterns with different angular ranges cause a possibility of a different choice of interpolation points for each pattern. A perfect position of the interpolation points is not so critical in MAUD because the interpolation is performed not on the raw experimental data, but on the residual after the intensity diffracted by all phases has been calculated and subtracted from the experimental pattern. Nevertheless, it is advantageous not to have interpolation points at positions of strong reflections.

For the refinement we used a periclase phase (MgO, cubic, $Fm\text{-}3m$) and substitute 25% Fe atoms for Mg to reach the correct ferropericlase composition. The calculated pattern [Figure 9(a), top] differs significantly from the experimental DAC patterns [Figure 9(a), bottom]. This is the result of the high-pressure condition (39.6 GPa) that shrinks the cell (a parameter) and enlarges peak positions 2θ. Thus the lattice parameter has to be adjusted manually before the refinement.

With only one image and four diffraction peaks, the coverage is largely insufficient to refine the OD without imposing sample symmetry. But in this DAC experiment texture should have axial symmetry around the compression direction. Before imposing axial symmetry we have to make sure that the compression direction (symmetry axis) is indeed in the center of the MAUD pole figure. We set the Z_M axis of our sample coincident with the compression axis by setting the χ angle (of the sample) value to 90° [Figure 1(b) for the MAUD angle conventions, see also Grässlin *et al.*, 2013]. The coverage (after this rotation) is shown in Figure 8(d). The "Sample → Sample position → Sample orientation" angles are sometimes refined, if data are sufficient (not possible in this case).

Note that poles to diffracting lattice planes are not perpendicular to the incident X-ray beam but deviate by θ (Bragg's law). This was barely noticeable for the coin (Part I, Figure 4) and for shale [Figure 1(c)], because diffraction angles were very small. In the MAUD "Texture plot" the coverage corresponds to the θ angle of the selected hkl in the list. Thus, in the standard rDAC geometry, lattice planes that are aligned perpendicular to the compression axis B [Figure 8(d)] do not diffract. Figure 8(e) shows the actual "Experimental intensity" distributions for three hkls, illustrating the slightly different coverage, depending on θ. In some cases, one may want to tilt the DAC to obtain an optimal coverage pattern.

C. Stress models

1. Macrostress

Lattice strain is due to the imposed anisotropic elastic stress and the elastic properties of the crystal. It is exhibited as sinusoidal oscillations in peak position with azimuth [Figure 9(b), bottom].

There are four models in MAUD that can be used to fit lattice strains, resulting in diffraction peak shifts. Two are "stress models" that convert macroscopic stress tensor components to lattice strains and then are used to compute reflection positions, using the provided elastic properties of the material. The other two models fit lattice strain distributions and leave it up to the user to calculate stresses in the end.

In axial compression experiments in the DAC, the anvils impose both hydrostatic stresses (pressure) and deviatoric stresses. The symmetric stress tensor σ_{ij} can be separated into hydrostatic σ_p and deviatoric D_{ij} stress components such that:

$$\sigma_{ij} = \begin{bmatrix} \sigma_p & 0 & 0 \\ 0 & \sigma_p & 0 \\ 0 & 0 & \sigma_p \end{bmatrix} + \begin{bmatrix} -t/3 & 0 & 0 \\ 0 & -t/3 & 0 \\ 0 & 0 & 2t/3 \end{bmatrix} \quad (1)$$
$$= \sigma_p + D_{ij},$$

where t is the axial stress component and provides lower bounds for the yield strength of the material (Singh, 1993; Singh *et al.*, 1998). Thus, during the refinement of the stresses, the deviatoric stresses should be constrained such that $\sigma_{11} = \sigma_{22}$ and $\sigma_{33} = -2\sigma_{11}$, where σ_{33} is the largest principal stress in the compression direction and is negative (corresponding to compression), according to the conventions in MAUD (component 33 of the stress is along the Z_M axis of the sample or in the center of the pole figure). For the analysis described here, only deviatoric stresses will be fit with the stress model. Hydrostatic stresses are accounted for by refining unit cell parameters, which in turn can be converted to pressure by utilizing an appropriate equation of state (see below). The reason for treating these separately is that deviatoric stresses will be calculated assuming a linear stress–strain relationship, which is only applicable for small strains. The volume changes of the unit cell due to pressure effects are significantly larger than those due to deviatoric stress, and it is best to use an equation of state that properly accounts for the nonlinearity of stress–strain dependence at larger compressions. On the other hand, for the analysis of the residual stresses, e.g., in engineering materials, where stress tensor components values are often within a 0.5 GPa range, it is appropriate to keep initial lattice parameters fixed. One should then only fit either stress or strain values (depending on the model of choice).

The four models in MAUD to fit stress–strain are: (1) a triaxial elastic stress, isotropic elastic material, $\sin^2\psi$ method (Noyan and Cohen, 1987); (2) the moment pole stress (Matthies, 1996 and Matthies *et al.*, 2001); (3) WSODF (Popa and Balzar, 2001); and (4) the radial diffraction in the DAC (Singh, 1993 and Singh *et al.*, 1998). Of these four models only the second and the fourth are appropriate for the type of analysis we want to do in this case. The first one does not take into account the texture and anisotropy of the sample and can be considered as a simplified version of the second, more complete model. The third one is used to extract a strain ODF, but here we are interested in finding both the hydrostatic and deviatoric parts of the pressure. It also requires much more orientational data than we have measured, as it needs to extract an entire strain ODF (with many coefficients) for each component of the strain tensor. In the following, we briefly describe how methods two and four work.

2. Moment pole stress

This model requires the elastic tensor (C_{ij}), corrected for pressure (and temperature, if necessary), for the material of interest. It is the most sophisticated model of the four and calculates diffraction elastic constants for each diffraction peak of the material, taking preferred orientation into account. It is able to use different micromechanical models similar to those used for calculating bulk polycrystal properties (e.g., Voigt, Reuss, Hill, GEO). The only difference is that for calculation of diffraction elastic constants, crystal properties should be averaged, using "moments" of OD or pole figures (corresponding values weighted by sine or cosine values of certain angles).

3. Radial diffraction in the DAC

This model is not a true "stress" model like the previous one. While the other models are more general and can be applied to more complicated deformation geometries, "Radial Diffraction in the DAC" can only be applied in the case of axial compression. This model fits a $Q(hkl)$ factor to each diffraction peak based on peak displacement and the angle to the principal stress axis. The main advantage of this model is that it allows the user to fit lattice strains for each peak separately, but retaining the mean cell parameter for the hydrostatic pressure computation, whereas previous models imply that all the displacements of diffraction peaks correspond to one macrostress tensor, or they are restricted by crystal symmetry. The "Triaxial Stress Isotropic E" and "Moment Pole Stress" models may fail if plastic anisotropy of the material is high. In the case of ferropericlase, some peaks exhibit much higher lattice strains than other peaks, and these two models may not be able to provide a satisfactory fit to the data.

4. Correcting Young's modulus and Poisson ratio or C_{ij} to pressure

As mentioned above, using the "Moment Pole Stress" or any stress fitting model (that requires the stiffness tensor or modulus), the elastic moduli must be corrected for pressure. Elastic moduli are pressure-dependent and often become larger as pressure increases or may display critical behavior near phase transitions. To correct elastic moduli for pressure, one will need an appropriate equation of state for the sample and a set of elastic moduli either calculated or experimentally determined for a range of pressures for the material. If the experiment is also at high temperature, one will need to correct for this as well. In addition, one must account for possible anisotropic thermal expansion of the sample.

The easiest way to correct the elastic moduli is to create a spreadsheet that uses an equation of state, such as a third-order

Birch–Murnaghan equation of state, to calculate pressure from the fitted unit-cell parameters. Next, plot each elastic coefficient (e.g., C_{11}, C_{22}, C_{33}, C_{12}, etc. or Young's modulus and Poisson's ratio) versus pressure. Once this is done, calculate a best-fit line to each of the elastic constants and determine the equation describing the pressure dependence for each constant. This will allow one to extrapolate or interpolate elastic moduli to any reasonable pressure [for $(Mg_{0.9}Fe_{0.1})O$ see Marquardt *et al.*, 2009]. Often a linear extrapolation is sufficient. Then one uses the pressure calculated from the unit-cell parameters to determine the appropriate value of the elastic moduli using the equations for the best-fit lines. One may need to perform several iterations of this before the unit cell parameter and stress values stabilize. The pressure should be calculated from the unit-cell parameter, correcting the elastic moduli to the pressure, inputting the corrected elastic moduli, and running the refinement. After doing this, one may notice that the unit cell parameter has changed. If so, the previous procedure should be repeated until the unit-cell parameter (and the corresponding pressure value) converge to a stable value.

Using the "Radial Diffraction in the DAC" model we can avoid such an iterative procedure and get directly the cell parameter as well as deviatoric strain and calculate the pressure from the equation of state.

D. Refinement

In this case, the refinement is quite complex involving strong texture and high stresses with limited data. We need to guide the refinement and accurately choose the parameters to refine. We try as much as possible to avoid refining unnecessary parameters. In summary, the refinement involves the following steps (see also Appendix 2):

- *Beam intensity and backgrounds*. We refine only beam intensity as we use an interpolated background.
- *Cell parameters*. Ferropericlase is cubic, so we need to refine only the unit-cell parameter *a*.
- *Texture*. As seen in Figure 10 the texture is fairly strong, thus we refine the texture early. With the E-WIMV method, we obtain first an OD without any sample symmetry to check and validate our hypothesis of imposing an axial symmetry [Figure 10(a)]. The pole figures look fairly symmetrical, even though only a single image with four diffraction peaks was recorded [Figure 8(d)]. This is because of the

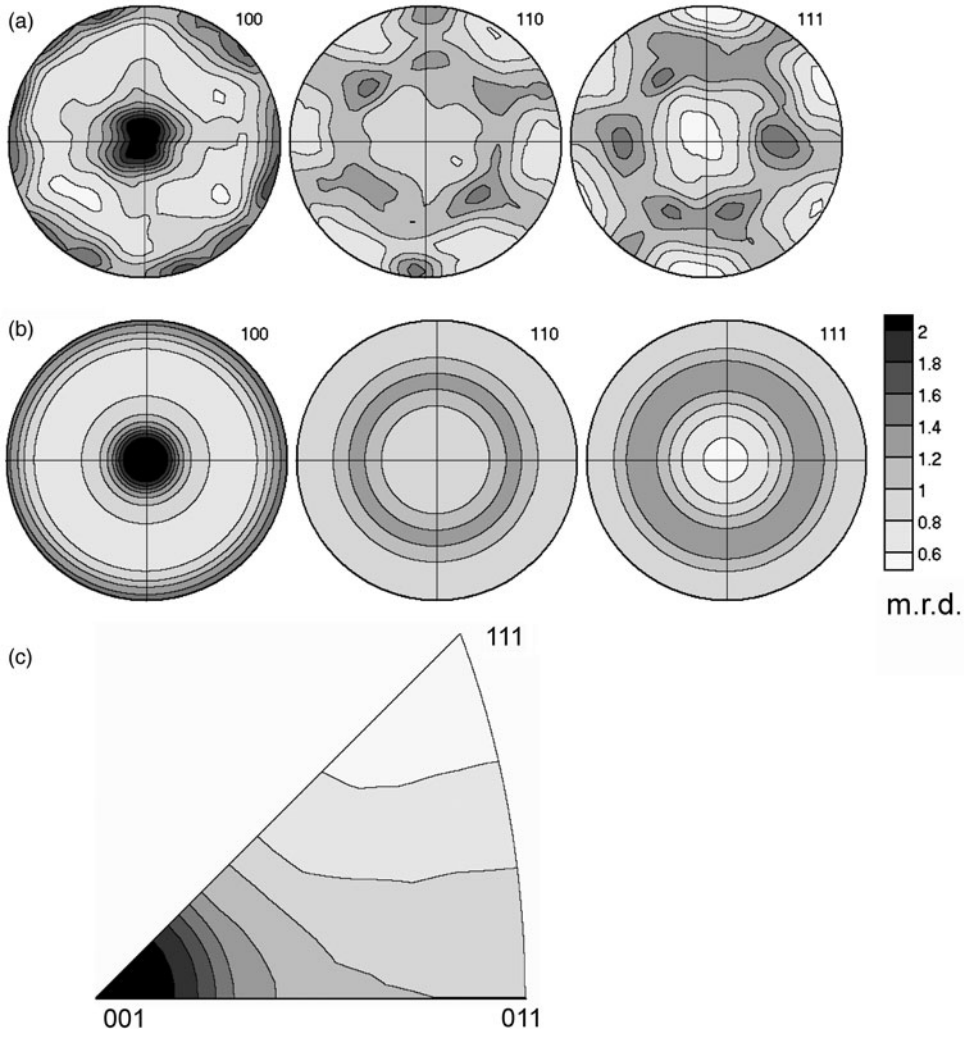

Figure 10. Texture information for ferropericlase at 39.6 GPa represented as pole figures (a, b) and inverse pole figures (c). (a) Pole figures without imposing sample symmetry. (b) Pole figures imposing fiber symmetry. (c) Inverse pole figure of the compression direction plotted by BEARTEX. Equal area projection, contours in multiples of a random distribution.

high cubic crystal symmetry that imposes constraints due to equivalent poles [three for (100), six for (110), and four for (111)]. For lower crystal symmetry, this would be much less complete. Once we verify that the texture and sample orientation is compatible with axial symmetry, we impose "fiber" sample symmetry [Figure 10(b)]. This greatly improves the effective pole figure coverage.

- *Crystallite size and r.m.s. microstrain*. Here we assume isotropic crystallite size and microstrain, which results in two refinable parameters. As mentioned earlier, with the coarse-grained LaB_6 standard, it was difficult to refine an accurate instrumental peak broadening. Thus obtained parameter values should be viewed as only qualitative.
- *Stress models*. For "Moment pole stress" we start with the elastic tensor values for ferropericlase at atmospheric pressure with $C_{11} = C_{22} = C_{33} = 279.5$ GPa, $C_{12} = C_{13} = C_{23} = 102.2$ GPa, $C_{44} = C_{55} = C_{66} = 142$ GPa, with all others equal to zero (Marquardt *et al.*, 2009) and we refine only the σ_{11} macrostress value. As an alternative for the "Radial Diffraction in the DAC" model, we refine $Q(hkl)$ factors of each diffraction peak in the refinement range (four parameters).
- *Beam center*. If reflection positions are not fitting well with the stress model and one still observes variations of peak position with angle η, refine the detector center errors (two parameters, x and y), since it may have changed during DAC positioning. In our case, it was not necessary.
- *Tilt of the DAC cell.* If there is evidence that the compression direction is tilted (not in this case), then we need to correct for this. In the "Radial Diffraction in the DAC" model, it is accomplished by refining the "Alpha" and "Beta" angles for a better fit. In the other stress-based models, the only option is to refine the sample orientation angles that define the coordinate system.
- *Heterogeneities of strain in the DAC cell.* In the "Plot 2D" display one may observe asymmetry in the texture between the lower and the upper half of the measured patterns display, while refined patterns demonstrate perfect symmetry. This may be due to heterogeneities of the sample in the DAC, e.g. some grains in the periphery of the cell are subjected to lower pressures and deviatoric stress. To accommodate this, one can use for the last refinement cycle only one half of the diffraction image. However, if only half the Debye ring is used, one should be sure to fix beam center and tilt parameters. Since axial symmetry of texture and stress state is imposed, the entire diffraction image is not needed to derive a reasonably accurate OD.

At the end of the analysis the refined cell parameter is 3.9866(1) Å and the corresponding volume is ≈ 63.36 Å^3. For radial diffraction the lattice parameter represents the strain resulting from the hydrostatic (pressure) component of the stress tensor. The derived pressure is ≈ 39.6 GPa and the final elastic tensor is $C_{11} = C_{22} = C_{33} \approx 624.4$ GPa, $C_{12} = C_{13} = C_{23} \approx 171.1$ GPa, and $C_{44} = C_{55} = C_{66} \approx 175.3$ GPa; the deviatoric macrostress σ_{11} component is ≈1.80(1) GPa. To calculate the equivalent t value in Eq. (1) we multiply by 3 this value to obtain 5.4 GPa.

In this analysis, we have been mainly concerned with preferred orientation, which, for axially symmetric textures, is conveniently displayed as inverse pole figures that represent the probability of the fiber axis relative to crystal coordinates. Figure 10(c) is the inverse pole figure of the compression direction after processing with BEARTEX. The texture is moderate, with a pole density maximum of ≈ 2.65 multiples of a random distribution, located close to 001 [Figure 10(d)], as previously observed (e.g., Merkel *et al.*, 2002; Kunz *et al.*, 2007; Lin *et al.*, 2009; Kaercher *et al.*, 2012). Quantitative texture information for the two models is summarized in Table III.

IV. CONCLUSIONS

Synchrotron X-rays provide a powerful method for quantitative texture analysis of materials. Depending on sample size, beam size and wavelength, small (<100 μm^3) to large volumes (>200 mm^3) can be analyzed, and different sample equipment can be used to impose different conditions on the sample (e.g., high pressure, high temperature, anisotropic stress). Compared to neutron diffraction, electron backscatter diffraction or pole-figure goniometry, data acquisition is fast, but data analysis is non-trivial. For complex polyphase materials (such as the shale sample) a careful manual procedure is necessary. Further complications arise for high-pressure experiments, where anisotropic stresses need to be accounted for. MAUD incorporates a set of methods able to account for preferred orientations, anisotropic stresses and microstructural characteristics of material. Here we provided only a brief overview of these and simplified step-by-step procedures that give general directions for the analysis, while highlighting some possible complications. Knowledge of the instrument, sample, and experimental setup is necessary to adjust these procedures to each specific case and obtain convincing results.

SUPPLEMENTARY MATERIALS

The supplementary material for this article can be found at http://www.journals.cambridge.org/PDJ

Supplementary Material Available from the Online Version.

Appendix 1. Step-by-step procedure for analysis of polymineralic shale.

Appendix 2. Step-by-step procedure for analysis of ferropericlase in diamond anvil cell.

ACKNOWLEDGEMENTS

This project was supported by NSF (EAR-0836402) and DOE (DE-FG02-05ER15637). We greatly appreciate access to beamline 11-ID-C at APS of Argonne National Laboratory and help from Chris Benmore and Yang Ren, as well as access to beamline 12.2.2. at ALS of Lawrence Berkeley Laboratory and help from Jason Knight. The tutorial was developed as part of a workshop at the Advanced Light Source in fall 2012, supported by CDAC, APS (BESSRC), NSF-COMPRES, ALS, and STONE-LANL. RV appreciates support of AYSS JINR (12-401-01). We appreciate input from many MAUD users, especially Juan Gomez-Barreiro, as well as the Editor Brian Toby and three reviewers that helped us improve the manuscript. We also acknowledge discussions with R. Jeanloz and A.K. Singh.

Bish, D. L. and Von Dreele, R. B. (**1989**). "Rietveld refinement of non-hydrogen atomic positions in kaolinite," Clays Clay Miner. **37**, 289–296.

Grässlin, J., McCusker, L. B., Baerlocher, C., Gozzo, F., Schmitt, B., and Lutterotti, L. (**2013**). "Advances in exploiting preferred orientation in the structure analysis of polycrystalline materials," J. Appl. Crystallogr. **46**, 173–180.

Gražulis, S., Chateigner, D., Downs, R. T., Yokochi, A. F. T., Quirós, M., Lutterotti, L., Manakova, E., Butkus, J., Moeck, P., and Le Bail, A. (**2009**). "Crystallography open database – an open access collection of crystal structures," J. Appl. Crystallogr. **42**, 726–729.

Gualtieri, A. F. (**2000**). "Accuracy of XRPD QPA using the combined Rietveld-RIR method," J. Appl. Crystallogr. **33**, 267–278.

Hornby, B. E. (**1998**). "Experimental laboratory determination of the dynamic elastic properties of wet, drained shales," J. Geophys. Res. **103**(B12), 29945–29964.

Kaercher, P., Speziale, S., Miyagi, L., Kanitpanyacharoen, W., and Wenk, H.-R. (**2012**). "Crystallographic preferred orientation in wüstite (FeO) through the cubic-to-rhombohedral phase transition," Phys. Chem. Miner. **39**, 613–626.

Kanitpanyacharoen, W., Wenk, H.-R., Kets, F., Lehr, B. C., and Wirth, R. (**2011**). "Texture and anisotropy analysis of Qusaiba shales," Geophys. Prospect. **59**, 536–556.

Kanitpanyacharoen, W., Kets, F. B., Wenk, H.-R., and Wirth, R. (**2012a**). "Mineral preferred orientation and microstructure in the Posidonia shale in relation to different degrees of thermal maturity," Clays Clay Miner. **60**, 315–329.

Kanitpanyacharoen, W., Merkel, S., Miyagi, L., Kaercher, P., Tomé, C. N., Wang, Y., and Wenk, H.-R. (**2012b**). "Significance of mechanical twinning in hexagonal metals at high pressure," Acta Mater. **60**, 430–442.

Kunz, M., Caldwell, W. A., Miyagi, L., and Wenk, H.-R. (**2007**). "*In situ* laser heating and radial synchrotron X-ray diffraction in a diamond anvil cell," Rev. Sci. Instrum. **78**, 063907, 1–6.

Le Bail, A., Duroy, H., and Fourquet, J. L. (**1988**). "*Ab initio* structure determination of $LiSbWO_6$ by X-ray powder diffraction," Mater. Res. Bull. **23**, 447–452.

Lin, J.-F., Wenk, H.-R., Voltolini, M., Speziale, S., Shu, J., and Duffy, T. (**2009**). "Deformation of lower mantle ferropericlase (Mg,Fe)O across the electronic spin transition," Phys. Chem. Miner. **37**, 585–592.

Lutterotti, L., Matthies, S., Wenk, H.-R., Schultz, A. S., and Richardson, J. W. (**1997**). "Combined texture and structure analysis of deformed limestone from time-of-flight neutron diffraction spectra," J. Appl. Phys. **81**, 594–600.

Lutterotti, L., Chateigner, D., Ferrari, S., Ricote, J. (**2004**). "Texture, residual stress and structural analysis of thin films using a combined X-ray analysis," Thin Solid Films **450**, 34–41.

Lutterotti, L., Bortolotti, M., Ischia, G., Lonardelli, I., and Wenk, H.-R. (**2007**). "Rietveld texture analysis from diffraction images," Z. Kristallogr. Suppl. **26**, 125–130.

Lutterotti, L., Voltolini, M., Wenk, H.-R., Bandyopadhyay, K., and Vanorio, T. (**2010**). "Texture analysis of turbostratically disordered Ca-montmorillonite," Am. Mineral. **95**, 98–103.

Lutterotti, L., Vasin, R. N., and Wenk, H.-R. (**2014**). "Rietveld texture analysis from synchrotron diffraction images: I. Basic analysis," Powder Diffr. **29**(1), 76–84.

Marquardt, H., Speziale, S., Reichmann, H. J., Frost, D. J., and Schilling, F. R. (**2009**). "Single-crystal elasticity of $(Mg_{0.9}Fe_{0.1})O$ to 81 GPa," Earth Planet. Sci. Lett. **287**, 345–352.

Matthies, S. (**1996**). "Moment pole figures in residual stress analysis," Text. Microstruct. **25**, 229–236.

Matthies, S. and Wenk, H.-R. (**2009**). "Transformations for monoclinic crystal symmetry in texture analysis," J. Appl. Crystallogr. **42**, 564–571.

Matthies, S., Vinel, G. W., and Helming, K. (**1987**). *Standard Distributions in Texture Analysis* (Akademie-Verlag, Berlin, Germany).

Matthies, S., Priesmeyer, H. G., and Daymond, M. R. (**2001**). "On the diffractive determination of single-crystal elastic constants using polycrystalline samples," J. Appl. Crystallogr. **34**, 585–601.

Merkel, S., Wenk, H.-R., Shu, J., Shen, G., Gillet, P., Mao, H.-K., and Hemley, R. J. (**2002**). "Deformation of polycrystalline MgO at pressures of the lower mantle," J. Geophys. Res. **107**, 1–17.

Miyagi, L., Kunz, M., Knight, J., Nasiatka, J., Voltolini, M., and Wenk, H.-R. (**2008**). "*In situ* phase transformation and deformation of iron at high pressure and temperature," J. Appl. Phys. **104**, 103510, 1–9.

Miyagi, L., Kanitpanyacharoen, W., Kaercher, P., Lee, K. K. M., and Wenk, H.-R. (**2010**). "Slip systems in $MgSiO_3$ post-perovskite: implications for D″ anisotropy," Science **329**, 1639–1641.

Miyagi, L., Kanitpanyacharoen, W., Raju, V., Kaercher, P., Knight, J., McDowell, A., Wenk, H. R., Williams, Q., and Zepeda, E. (**2013**). "Combined resistive and laser heating technique for in situ radial X-ray diffraction in the diamond anvil cell at high pressure experiments and temperature". Rev. Sci. Instr. **84**, 025118, 1–9.

Noyan, I. C. and Cohen, J. B. (**1987**). *Residual Stress: Measurement by Diffraction and Interpretation* (Springer-Verlag, Berlin).

Plançon, A., Tsipurski, S. I., and Drits, V. A. (**1985**). "Calculation of intensity distribution in the case of oblique texture electron diffraction," J. Appl. Crystallogr. **18**, 191–196.

Popa, N. C. (**1992**). "Texture in Rietveld refinement," J. Appl. Crystallogr. **25**, 611–616.

Popa, N. C. and Balzar, D. (**2001**). "Elastic strain and stress determination by Rietveld refinement: generalized treatment for textured polycrystals for all Laue classes," J. Appl. Crystallogr. **34**, 187–195.

Singh, A. K. (**1993**). "The lattice strains in a specimen (cubic system) compressed nonhydrostatically in an opposed anvil device," J. Appl. Phys. **73**, 4278–4286.

Singh, A. K., Mao, H.-K., Shu, J., and Hemley, R. J. (**1998**). "Estimation of single-crystal elastic moduli from polycrystalline X-ray diffraction at high pressure: application to FeO and iron," Phys. Rev. Lett. **80**, 2157–2160.

Sonneveld, E. J. and Visser, J. W. (**1975**). "Automatic collection of powder data from photographs," J. Appl. Crystallogr. **8**, 1–7.

Ufer, K., Roth, G., Kleeberg, R., Stanjek, H., Dohrmann, R., and Bergmann, J. (**2004**). "Description of X-ray powder pattern of turbostratically disordered layer structures with a Rietveld compatible approach," Z. Kristallogr. **219**, 519–527.

Vasin, R., Wenk, H.-R., Kanitpanyacharoen, W., Matthies, S., and Wirth, R. (**2013**). "Anisotropy of Kimmeridge shale," J. Geophys. Res. **118**, 1–26.

Wenk, H.-R., Matthies, S., Donovan, J., and Chateigner, D. (**1998**). "BEARTEX: a Windows-based program system for quantitative texture analysis," J. Appl. Crystallogr. **31**, 262–269.

Wenk, H.-R., Matthies, S., Hemley, R. J., Mao, H.-K., and Shu, J. (**2000**). "The plastic deformation of iron at pressures of the Earth's inner core," Nature **405**, 1044–1047.

Wenk, H.-R., Ischia, G., Nishiyama, N., Wang, Y., and Uchida, T. (**2005**). "Texture development and deformation mechanisms in ringwoodite," Phys. Earth Planet. Inter. **152**, 191–199.

Wenk, H.-R., Lonardelli, I., Merkel, S., Miyagi, L., Pehl, J., Speziale, S., and Tommaseo, C. E. (**2006**). "Deformation textures produced in diamond anvil experiments, analyzed in radial diffraction geometry," J. Phys. Condens. Matter **18**, S933–947.

Wenk, H.-R., Voltolini, M., Kern, H., Popp, T., and Mazurek, M. (**2008**). "Anisotropy in shale from Mont Terri," The Leading Edge **27**, 742–748.

Wenk, H. R., Kaercher, P., Kanitpanyacharoen, W., Zepeda-Alarcon, E., and Wang, Y. (**2013**). "Orientation relations during the $\alpha - \omega$ phase transition of zirconium – *in situ* texture observations at high pressure and temperature," Phys. Rev. Lett. **111**, 195701.